Proceedings of ASME 2019 Conference on Smart Materials, Adaptive Structures and Intelligent Systems
SMASIS 2019
Sept 9-11, 2019, Louisville, KY USA

SMASIS2019-5534

A HIGH-FIDELITY DYNAMIC MODEL FOR ORIGAMI BASED ON ISO-PARAMETRIC ABSOLUTE NODAL COORDINATE FORMULATION (ISO-ANCF)

Jiayue Tao* and Suyi Li
Department of Mechanical Engineering
Clemson University, Clemson, SC, USA

ABSTRACT

Origami-inspired structures and material systems have been used in many engineering applications because of their unique kinematic and mechanical properties induced by folding. However, accurately modeling and analyzing origami folding and the associated mechanical properties are challenging, especially when large deformation and dynamic responses need to be considered. In this paper, we formulate a high-fidelity model—based on the iso-parametric Absolute Nodal Coordinate Formulation (ANCF)—for simulating the dynamic folding behaviors of origami involving large deformation. The center piece of this new model is the characterization of crease deformation. To this end, we model the crease using rotational spring at the nodes. The corresponding folding angle is calculated based on the local surface normal vectors. Compared to the currently popular analytical methods for analyzing origami, such as the rigid-facet and equivalent bar-hinge approach, this new model is more accurate in that it can describe the large crease and facet deformation without imposing many assumptions. Meanwhile, the ANCF based origami model can be more efficient computationally compared to the traditional finite element simulations. Therefore, this new model can lay down the foundation for high-fidelity origami analysis and design that involve mechanics and dynamics.

Keywords: Origami Dynamics, High-fidelity Modeling, Absolute Nodal Coordinate formulation (ANCF)

1. INTRODUCTION

Origami is the ancient art of folding paper into decorative shapes. Over the past several decades, this art has been transformed into a framework for designing and fabricating engineered systems such as deployable structures [1] and mechanical metamaterials [2]. Such a development in origami application calls for robust and computationally efficient models to simulate and analyze the deformations induced by folding. To this end, many analytical methods have been proposed with different degrees of success.

For rigid origamis that do not induce any facet deformation during folding, one can obtain a closed form solution for folding by assuming rigid facets and hinge-like creases, essentially turning the origami into 3D linkage mechanisms [3]. However, this method is limited to few origami designs such as the Miura-*ori* and its derivatives [4][5]. Moreover, it cannot describe any facet deformations like bending and twisting, which are inevitable or even desired in realistic origami applications.

To accommodate the facet deformations, several bar-hinge methods have been developed. For example, Resch and Christiansen exploited linear elastic rotational hinges for the folding creases, and modelled each facet using a plane stress element [6]. Schenk [7] and later Li et al. [8] applied this bar-hinge method to Miura-*ori* sheets to examine their fundamental modes of deformation via eigen-analysis. However, bar-hinge methods were initially intended for problems of infinitesimal deformation since they used linear elasticity formulation [9][10]. To address this limitation, Liu et al. [11] and Gillman et al. [12] developed nonlinear bar-hinge models that considered both geometric and material nonlinearities. These nonlinear models are significantly more capable, but they still only provide insights into the global behavior of origami folding and cannot analyze the local origami deformations with a high resolution.

Besides the reduced-order analytical models, finite element methods (FEM) were also used to simulate origami folding. In FEM, the facets are typically meshed using shell elements. The challenge here is to properly model the creases because they exhibit highly concentrated stress and strain during folding. To our best of knowledge, two crease modeling techniques have been developed so far [13]. One is to use additional "hinge connection

*Address all correspondence to this author: jiayuet@g.clemson.edu

elements" to join the overlapping shell element nodes along the creases, and then assign rotational stiffness to these hinge elements. For example, Zhou et al. modeled the crease as hinge joints with a revolute-type connector element inserted at the center of the crease [14]. Filipov et al. [15] modeled the crease as elastic rotational springs at the nodes of interconnected shell elements (Figure 1.) and the spring coefficient is assumed independent of folding angle and scale linearly with the fold length. The other method of modeling the creases in FEM is to use a refined shell element mesh near the creases and assign reduced stiffness and strength properties [16]. Compared to the bar-hinge models, the finite element models can provide more information like the stress/strain distribution near the creases and localized buckling in the facets. However, they are computationally expensive, and more importantly, the localized instabilities caused by large element deformation can prevent the simulations to convergence quickly.

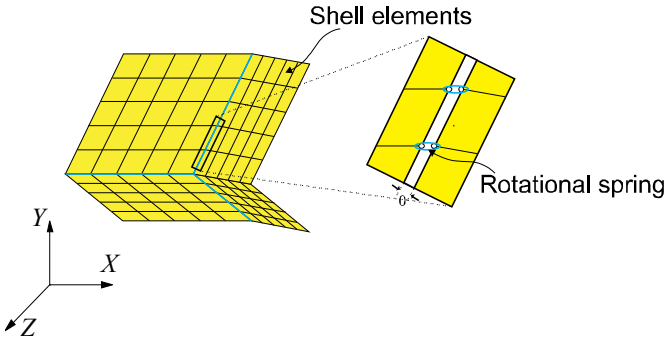

Figure 1. Traditional finite element formulations of origami. Here, the facet is modeled as conventional shell elements, whereas the crease is treated as linear elastic rotational springs at the nodes of interconnected shell elements. Figure adapted with permission [14].

Therefore, the objective of this study is to propose and formulate a high-fidelity dynamic model of origami using a *finite-element inspired* approach. Instead of meshing the origami sheets with many elements, we propose to exploit the tessellated nature of origami and treat each facet as one shell element. To ensure the accuracy, we adopt the iso-parametric Absolute Nodal Coordination Formulation (referred to as iso-ANCF hereafter), which is efficient and robust for dynamic analysis of structure under large deformations and rotations. To complete this new model, we develop a new crease model by treating them as rotational springs at the crease nodes. Based on this, we also formulate a new tangent stiffness matrix of the creases and provide the final equations of motion for origami folding. Compared to existing nonlinear bar-hinge model [11], our model can be more accurate for dynamic analysis of complex origami structures with curved crease patterns. Also, it can be more computationally efficient than that by using tradition FEM. Therefore, the proposed model could strike a balance between accuracy and computational efficiency, thus facilitate the future advancement of origami design and analysis.

The remainder of this paper is organized as follows. Section 2 briefly reviews the basics of ANCF. Section 3 constructs the new model for origami folding using the iso-ANCF method, with special attentions to the modeling of origami crease. Governing equation of motion is formulated at the end of this section. Conclusions are drawn in Section 4.

2. FUNDAMENTALS OF ANCF

Traditional finite element methods use displacement and rotation as the nodal coordinates, but they turn out to be numerically unstable and inefficient when large deformations or rotations occur. To address this issue, Mikkola and Shabana proposed Absolute Nodal Coordinate Formulation (ANCF) by using position and position gradients as the nodal coordinates [17]. In ANCF, the global position field is defined as [18]

$$\mathbf{r} = \mathbf{S}(x, y)\mathbf{e}, \tag{1}$$

where x, y are element local coordinates, as shown in Figure 2A. $\mathbf{r}$ is the global position vector based on global coordinates. $\mathbf{S}(x, y)$ is the element shape function matrix based on local coordinates; $\mathbf{e}$ is the vector of nodal coordinates that consist of nodal position and position gradients as shown in Figure 2B, it is formulated as,

$$\mathbf{e} = \begin{bmatrix} \mathbf{e}^1 & \mathbf{e}^2 & \mathbf{e}^3 \end{bmatrix}^T. \tag{2}$$

For each node (n), this vector is given by

$$\mathbf{e}^n = = \begin{bmatrix} \mathbf{r}^n & \mathbf{r}_x^n & \mathbf{r}_y^n \end{bmatrix} = \begin{bmatrix} \mathbf{r}^n & \dfrac{\partial \mathbf{r}^n}{\partial x} & \dfrac{\partial \mathbf{r}^n}{\partial y} \end{bmatrix}. \tag{3}$$

Compared to the traditional finite element method, ANCF is robust in analyzing the large structural deformation and rotation. Firstly, ANCF directly uses position gradients at the nodes rather than rotations, which means no magnitude limit of the rotation within ANCF elements [17]. This reduces the number of elements required to represent complex shell structures. Secondly, most existing finite element methods for analyzing the large deformation and rotation of plates and shells generate nonlinear mass matrix, whereas the mass matrix in ANCF is constant. This allows the use of efficient algorithms for solving dynamic equations of motion [19][20]. Thirdly, ANCF uses the continuum mechanics approach where Green-Lagrange strain tensor is used to describe the nonlinear strain-displacement relationships. As a result, this formulation can inherently account for all geometric nonlinearities.

In the next section, we formulate a high-fidelity dynamics model for origami by using a variation of ANCF: iso-parametric ANCF (or simply iso-ANCF). Here, the inter-element continuity conditions will be carefully handled to simulate behavior of creases, as explained in Section 3.2.

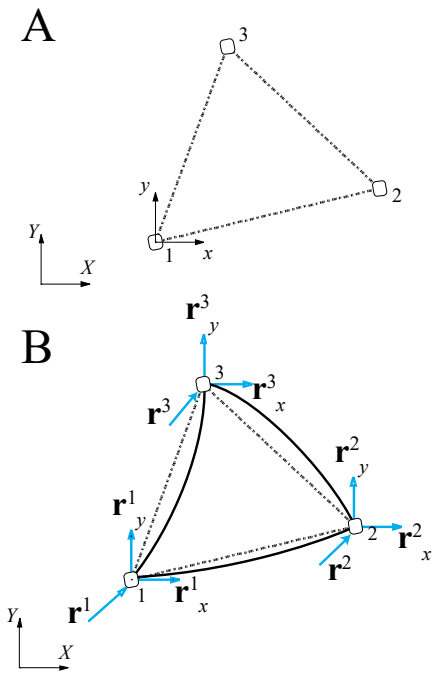

Figure 2. Triangular element parameterization in ANCF method. A. Local and global coordinate systems for ANCF element. B. The formulation of vector of the nodal coordinates in ANCF method, where the gradient vectors are defined based on element local coordinates.

3. ISO-PARAMETRIC ANCF FOR ORIGAMI FOLDING

3.1 Governing Kinematic Relationship

3.1.1 Triangular Element Parametrization

Pappalardo et al. [21] furtherly developed iso-ANCF formulation based on traditional ANCF. This formulation treats elements as iso-parametric ones so that the same shape functions can be used to describe their geometry and displacement. The nodal position gradients are defined based on the iso-parametric coordinates instead of element spatial coordinates. In this way, it becomes easier to construct shape functions that satisfy the consistency requirements for higher order elements with curved boundaries. Furthermore, the integrals appeared in the dynamic equations of motion becomes easier to evaluate because they can be transformed into the reference domain as shown in Figure 4where the shell elements have simple shapes—and calculated by the Gaussian quadrature rule.

In the 3D domain, a triangular element with curved sides can be parametrized by three iso-parametric coordinates: ξ, η, and ζ. Out of the three coordinates, only two are independent so they satisfy the constraint equation $\xi+\eta+\zeta=1$ [21]. For example, one can use η_i and ζ_i as the independent coordinates with the origin at node 1, and the iso-parametric coordinate ξ can be determined by constraint equation $\xi=1-\eta_i-\zeta_i$ (Figure 3A). Here the subscript "i" stands for independent coordinates. An important advantage by using this set of coordinates is that the position gradient vectors can be defined as tangents to the triangle sides at the nodes (Figure 3B). This is crucial for modeling the creases, as we will detail in Section 3.2.

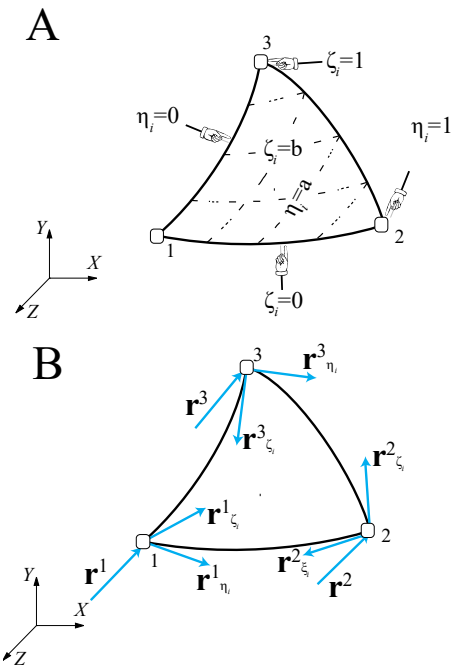

Figure 3. Triangular element parameterization in Iso-ANCF method. A. Independent iso-parametric coordinate system with the origin at node 1. Here, the constraint equation $\xi=1-\eta_i-\zeta_i$ applies. Any point in the element can be uniquely determined by independent iso-parametric coordinates $(\eta_i=a,\ \zeta_i=b)$, where $a,b\in[0,1]$. B. The formulation of vector of the nodal coordinates in iso-ANCF method, where the gradient vectors are defined based on independent iso-parametric coordinates.

The position field of the iso-ANCF triangle element can be written as

$$\mathbf{r}=\mathbf{S}(\xi_i,\eta_i,\zeta_i)\mathbf{e}, \tag{4}$$

where $\mathbf{S}$ is the shape function matrix based on independent iso-parametric coordinates, which is

$$\mathbf{S}=\left[s_1\mathbf{I}\ s_2\mathbf{I}\ s_3\mathbf{I}\ s_4\mathbf{I}\ s_5\mathbf{I}\ s_6\mathbf{I}\ s_7\mathbf{I}\ s_8\mathbf{I}\ s_9\mathbf{I}\right]. \tag{5}$$

Here, $\mathbf{I}$ is the 3×3 identity matrix; and $\mathbf{e}$ is the vector of the nodal coordinates which can be written as

$$\mathbf{e} = \left[\mathbf{r}^1 \ \mathbf{r}^1_{\eta_i} \ \mathbf{r}^1_{\zeta_i} \ \mathbf{r}^2 \ \mathbf{r}^2_{\zeta_i} \ \mathbf{r}^2_{\xi_i} \ \mathbf{r}^3 \ \mathbf{r}^3_{\xi_i} \ \mathbf{r}^3_{\eta_i} \right]^T, \tag{6}$$

where $\mathbf{r}_{\xi_i} = \partial \mathbf{r} / \partial \xi_i$, $\mathbf{r}_{\eta_i} = \partial \mathbf{r} / \partial \eta_i$, and $\mathbf{r}_{\zeta_i} = \partial \mathbf{r} / \partial \zeta_i$ are the nodal position gradients defined with respect to the independent isoparametric coordinates, and superscripts 1, 2, 3 refer to the element corner nodes ordered counterclockwise. The shape functions s_j ($j = 1, 2, ..., 9$) are included in the Appendix A.

3.1.2 Formulation of the Deformation Gradient

A key quantity in finite deformation analysis is the deformation gradient tensor **F**. It describes the relative spatial positions of two neighboring particles in the current configuration in terms of their relative spatial positions in the initial configuration, so the deformation gradient is central to the description of strain tensors [17][22].

In the initial configuration (Figure 4), the global position vector of an arbitrary point in the triangle element is defined as

$$\mathbf{X} = \mathbf{S}\mathbf{e}_0, \tag{7}$$

where **S** is the shape function matrix of the iso-ANCF triangle element defined in (5); and $\mathbf{e}_0$ is the vector of nodal coordinates in the initial configuration.

In the current configuration (Figure 4), the global position vector of an arbitrary point in the element is defined as

$$\mathbf{r} = \mathbf{S}\mathbf{e}, \tag{8}$$

where **S** is the same shape function matrix of the iso-ANCF; and **e** is the vector of nodal coordinates in the current configuration. Hence, the deformation gradient tensor **F** is defined as

$$\mathbf{F} = \frac{\partial \mathbf{r}}{\partial \mathbf{X}} = \begin{bmatrix} \frac{\partial \mathbf{S}_1}{\partial X}\mathbf{e} & \frac{\partial \mathbf{S}_1}{\partial Y}\mathbf{e} & \frac{\partial \mathbf{S}_1}{\partial Z}\mathbf{e} \\ \frac{\partial \mathbf{S}_2}{\partial X}\mathbf{e} & \frac{\partial \mathbf{S}_2}{\partial Y}\mathbf{e} & \frac{\partial \mathbf{S}_2}{\partial Z}\mathbf{e} \\ \frac{\partial \mathbf{S}_3}{\partial X}\mathbf{e} & \frac{\partial \mathbf{S}_2}{\partial Y}\mathbf{e} & \frac{\partial \mathbf{S}_3}{\partial Z}\mathbf{e} \end{bmatrix}, \tag{9}$$

where $\mathbf{S}_i$ is i^{th} row of the shape function matrix; and X, Y, Z are the global coordinates in the reference (initial) configuration.

The matrix of deformation gradients consists of derivatives of the shape functions with respect to the global coordinates, therefore, the derivatives $\partial s_k / \partial X$, $\partial s_k / \partial Y$, and $\partial s_k / \partial Z$ need to be related to $\partial s_k / \partial \xi_i$, $\partial s_k / \partial \eta_i$, and $\partial s_k / \partial \zeta_i$, where s_k are the scalar components in Equation (5). Using chain rule, one can obtain

$$\begin{bmatrix} \frac{\partial s_k}{\partial \xi_i} \\ \frac{\partial s_k}{\partial \eta_i} \\ \frac{\partial s_k}{\partial \zeta_i} \end{bmatrix} = \begin{bmatrix} \frac{\partial X}{\partial \xi_i} & \frac{\partial Y}{\partial \xi_i} & \frac{\partial Z}{\partial \xi_i} \\ \frac{\partial X}{\partial \eta_i} & \frac{\partial Y}{\partial \eta_i} & \frac{\partial Z}{\partial \eta_i} \\ \frac{\partial X}{\partial \zeta_i} & \frac{\partial Y}{\partial \zeta_i} & \frac{\partial Z}{\partial \zeta_i} \end{bmatrix} \begin{bmatrix} \frac{\partial s_k}{\partial X} \\ \frac{\partial s_k}{\partial Y} \\ \frac{\partial s_k}{\partial Z} \end{bmatrix} = \mathbf{J}^T \begin{bmatrix} \frac{\partial s_k}{\partial X} \\ \frac{\partial s_k}{\partial Y} \\ \frac{\partial s_k}{\partial Z} \end{bmatrix}. \tag{10}$$

As shown in Figure 4, the transformation between scaled straight element in reference/unit configuration and distorted element in initial configuration is expressed in the element trasformation matrix(Jacobian matrix, **J**), which defines the mapping between the isoparametric coordinates and the global coordinates. It can be calculated as

$$\mathbf{J} = \frac{\partial \mathbf{X}}{\partial \boldsymbol{\chi}} = \begin{bmatrix} \frac{\partial \mathbf{S}_1}{\partial \xi_i}\mathbf{e}_0 & \frac{\partial \mathbf{S}_1}{\partial \eta_i}\mathbf{e}_0 & \frac{\partial \mathbf{S}_1}{\partial \zeta_i}\mathbf{e}_0 \\ \frac{\partial \mathbf{S}_2}{\partial \xi_i}\mathbf{e}_0 & \frac{\partial \mathbf{S}_2}{\partial \eta_i}\mathbf{e}_0 & \frac{\partial \mathbf{S}_2}{\partial \zeta_i}\mathbf{e}_0 \\ \frac{\partial \mathbf{S}_3}{\partial \xi_i}\mathbf{e}_0 & \frac{\partial \mathbf{S}_2}{\partial \eta_i}\mathbf{e}_0 & \frac{\partial \mathbf{S}_3}{\partial \zeta_i}\mathbf{e}_0 \end{bmatrix}. \tag{11}$$

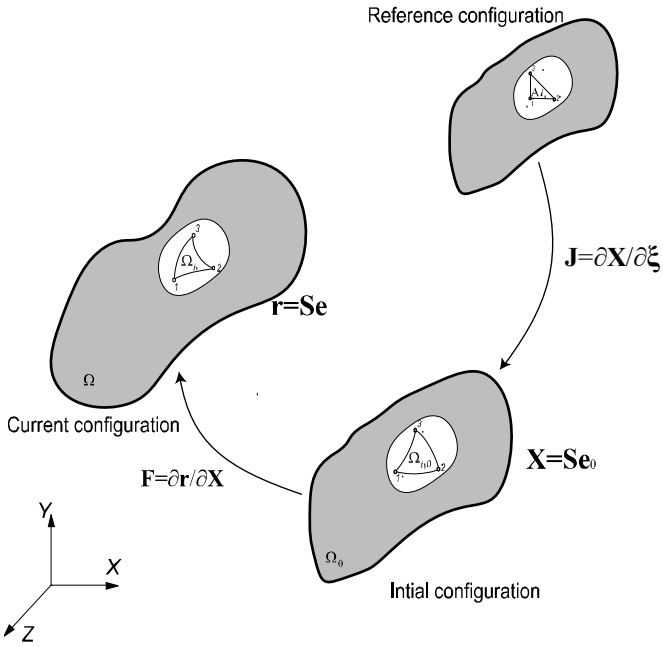

Figure 4. General motion of a spatial continuum body.

The inverse of both sides of Equation (10) is

$$\begin{bmatrix} \frac{\partial s_k}{\partial X} \\ \frac{\partial s_k}{\partial Y} \\ \frac{\partial s_k}{\partial Z} \end{bmatrix} = (\mathbf{J}^T)^{-1} \cdot \begin{bmatrix} \frac{\partial s_k}{\partial \xi_i} \\ \frac{\partial s_k}{\partial \eta_i} \\ \frac{\partial s_k}{\partial \zeta_i} \end{bmatrix} \tag{12}$$

By inserting (5) into (11) to obtain **J**, which is then substituted into (12) and (9), one can obtain the expression of the deformation gradient **F** in terms of **e**.

3.2 Modeling of Origami Crease

Liu et al. [11] presented a nonlinear bar-hinge model, in which the creases are treated as rotational springs that can store potential energy as they fold. The corresponding folding angle is defined as the dihedral angle between two neighboring facets, which are defined by three bar elements. This crease description is valid only if the facets are planar or nearly planar as the origami deforms, i.e., it restricts the magnitude of facet deformation. Moreover, when it comes to complex origami structures with curved crease pattern, such as in Earwig wing [23], it is impractical to model it only by bar elements.

Based on the iso-ANCF method proposed in this paper, the crease is modeled by rotational spring at the nodes and the corresponding folding angle is calculated based on the local surface normal vectors at these nodes (Figure 5).

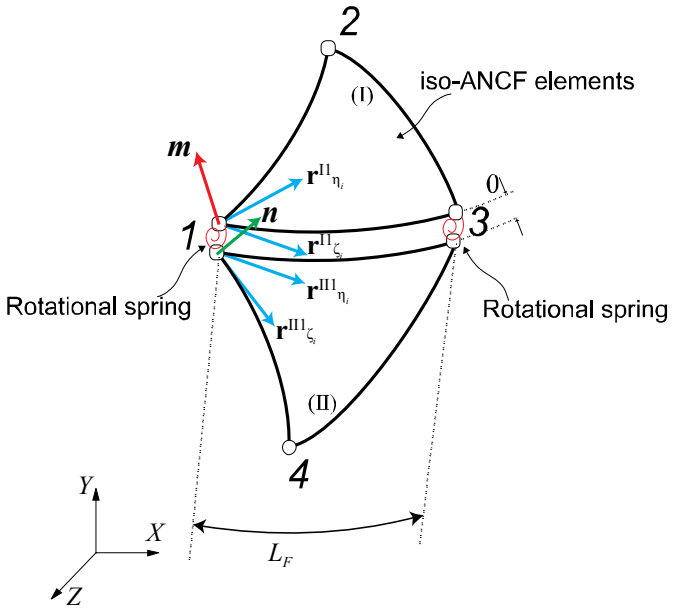

Figure 5. Modeling of origami crease. Here, the facet is modeled as iso-ANCF elements, whereas the crease is modeled by rotational springs at the nodes. The degree of rotation is measured by the folding angle θ, which is defined based on the local surface normal vectors at the nodes 1 and 3 of facet element I and II, respectively.

The folding energy of the crease is defined as

$$U_f = \sum_{j=1}^{l} U_{f,j} = \sum_{j=1}^{l} \frac{1}{2} k_f \left(\theta_j - \theta_{j,0}\right)^2 \tag{13}$$

where l is the number of nodes with rotational springs along the crease (in this model, $l = 2$), and $U_{f,j}$ denotes the folding energy of the j^{th} rotational spring; θ_j is the degree of rotation, aka. the folding angle at the j^{th} rotational spring, and $\theta_{j,0}$ is the corresponding initial stress-free folding angle, which could be calculated by using basic geometric relations in the initial configuration.

The localized stiffness of the crease is simply defined as

$$k_l = \frac{L_F}{L^*} k \tag{14}$$

where k is the bending modulus of the sheet defined as $k = Et^3/12(1-\nu^2)$, E, ν is Young's modulus and Poisson's ratio of the sheet. L^* is length scale factor (in units of length), which defines the relative stiffness of the fold based on the material, fabrication, and geometric properties [25].

As shown in Figure 5, the crease is modeled by two rotational springs at nodes 1 and 3. Half of the stiffness from (14) is distributed to each rotational spring, that is, the stiffness of rotational spring at the nodes 1 and 3 is defined as

$$k_f = \frac{1}{2} k_l = \frac{1}{2} \frac{L_F}{L^*} k \tag{15}$$

The definition of folding angle θ_j of the j^{th} rotational spring can be given by

$$\theta_j = \arccos\left(\frac{\boldsymbol{m} \cdot \boldsymbol{n}}{\|\boldsymbol{m}\| \cdot \|\boldsymbol{n}\|}\right) \mod 2\pi, \tag{16}$$

where the symbol 'mod' means modulo operation; $\boldsymbol{m}$ and $\boldsymbol{n}$ are the local surface normal vectors at the j^{th} rotational spring, that is

$$\boldsymbol{m} = \mathbf{r}_{\eta_i}^{\text{I1}} \times \mathbf{r}_{\zeta_i}^{\text{I1}}, \quad \boldsymbol{n} = \mathbf{r}_{\zeta_i}^{\text{II1}} \times \mathbf{r}_{\eta_i}^{\text{II1}}. \quad \text{at node 1} \tag{17}$$

$$\boldsymbol{m} = \mathbf{r}_{\xi_i}^{\text{I3}} \times \mathbf{r}_{\eta_i}^{\text{I3}}, \quad \boldsymbol{n} = \mathbf{r}_{\xi_i}^{\text{II3}} \times \mathbf{r}_{\zeta_i}^{\text{II3}}. \quad \text{at node 3} \tag{18}$$

Here, the operator '$\times$' between two vectors is the cross product.

In the framework of iso-ANCF method, the continuity equations of the rotational spring (aka. linear hinge constraint) at nodes 1 and 3 can be expressed as

$$\mathbf{r}^{\text{I1}} = \mathbf{r}^{\text{II1}}, \qquad \mathbf{r}_{\zeta_i}^{\text{I1}} = \mathbf{r}_{\eta_i}^{\text{II1}}, \tag{19}$$

$$\mathbf{r}^{\mathrm{I3}} = \mathbf{r}^{\mathrm{II3}}, \qquad \mathbf{r}_{\xi_i}^{\mathrm{I3}} = \mathbf{r}_{\xi_i}^{\mathrm{II3}}. \tag{20}$$

It is worth highlighting that by using the iso-ANCF method, the definition of folding angle θ in equation (16) is valid for origami with curved crease pattern. This is a clear advantage compared to the currently popular bar-hinge models, which assume that the facet defined by three bar elements must remain planar. Furthermore, iso-ANCF allows us to model complex shell structures by using a small number of elements.

3.3 Equations of Motion

To derive the governing dynamic equations of motion of origami folding based on iso-ANCF method, we employ the Lagrange equations

$$\frac{\mathrm{d}}{\mathrm{d}t}\left(\frac{\partial T}{\partial \dot{\mathbf{e}}}\right) + \left(\frac{\partial U}{\partial \mathbf{e}} + \frac{\partial U_f}{\partial \mathbf{e}}\right) = \frac{\partial W_{ext}}{\partial \mathbf{e}}. \tag{21}$$

In the subsections below, we detail the derivation of the terms in (21), separately.

3.3.1 Work done by the external force

As shown in Figure 6, the definition of work done by distributed external force vector $\boldsymbol{f}_i$ (i.e. the surface traction vector for thin shell structure) is

$$W_{ext} = \sum_{i=1}^{m} \int_{\Omega_i} \boldsymbol{f}_i \cdot \mathbf{r}_i \mathrm{d}\Omega_i, \tag{22}$$

where m is the total number of facet elements; $\mathbf{r}_i$ is the global position vector of element i. Based on the fundamental of continuum mechanics [22], equation (22) can be rewritten as

$$W_{ext} = \sum_{i=1}^{m} \int_{\Omega_{i,0}} \boldsymbol{f}_{i,0} \cdot \mathbf{r}_i \mathrm{d}\Omega_{i,0}. \tag{23}$$

Here, $\boldsymbol{f}_i \mathrm{d}\Omega_i = \boldsymbol{f}_{i,0}\mathrm{d}\Omega_{i,0}$ is applied. $\mathrm{d}\Omega_i$ and $\mathrm{d}\Omega_{i,0}$ is the infinitesimal surface area of facet element i in current and initial configuration, respectively. $\boldsymbol{f}_i$ and $\boldsymbol{f}_{i,0}$ is the external force vector defined in current and initial configuration, respectively.

The integration of external work W_{ext} needs to be performed over spatial domain in the initial configuration, which can have an irregular and complex shape. Hence, it is easier to perform the integration over the corresponding reference domain as shown in Figure 6, where $\mathrm{A}_i = \left\{(\xi,\eta,\zeta) \mid 0 \le \xi,\eta,\zeta \le 1, \xi+\eta+\zeta = 1\right\}$. The mapping between the two domains is [18]

$$\mathrm{d}\Omega_{i,0} = \left|\mathbf{J}\right| \mathrm{dA}_i \tag{24}$$

Here $\mathbf{J}$ is the Jacobian matrix in (11). So equation (22) can be updated as

$$W_{ext} = \sum_{i=1}^{m} \int_{\mathrm{A}_i} \mathbf{r}_i^T \boldsymbol{f}_{i,0} \left|\mathbf{J}\right| \mathrm{dA}_i. \tag{25}$$

The generalized external forces vector can be calculated as

$$\mathbf{Q}_g = \frac{\partial W_{ext}}{\partial \mathbf{e}} = \sum_{i=1}^{m} \int_{\mathrm{A}_i} \left(\frac{\partial \mathbf{r}_i}{\partial \mathbf{e}}\right)^T \boldsymbol{f}_{i,0} \left|\mathbf{J}\right| \mathrm{dA}_i. \tag{26}$$

Here, the global position gradient vector can be written as

$$\frac{\partial \mathbf{r}}{\partial \mathbf{e}} = \frac{\partial (\mathbf{S}\mathbf{e})}{\partial \mathbf{e}} = \mathbf{S}. \tag{27}$$

Hence,

$$\mathbf{Q}_g = \sum_{i=1}^{m} \int \mathbf{S}^T \boldsymbol{f}_{i,0} \left|\mathbf{J}\right| \mathrm{dA}_i. \tag{28}$$

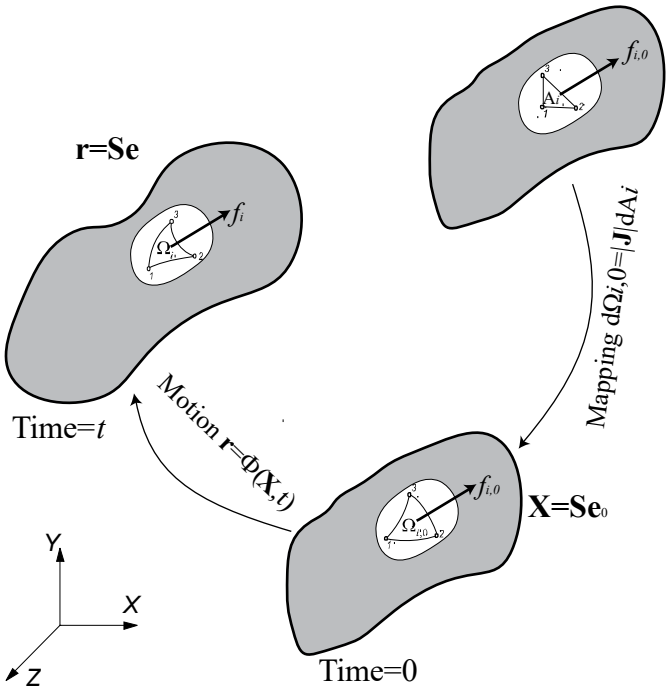

Figure 6. Work done by the external force. Here, the origami is modeled as thin shell structure, and we assume no body force is applied when origami deforms.

3.3.2 Facet strain energy

Here, we assume the origami material is linearly elastic, but the deformation is finite so geometric nonlinearity must be taken into consideration [17]. We use Kirchhoff plate theory with nonlinear strain-displacement relationships to obtain elastic forces.

The definition of strain energy of the facet elements can be written as follows

$$U=\sum_{i=1}^{m}\frac{1}{2}\int_{\Omega_{i,0}}\boldsymbol{\varepsilon}_i^T\boldsymbol{E}\boldsymbol{\varepsilon}_i\mathrm{d}\Omega_{i,0}+\frac{1}{2}\int_{\Omega_{i,0}}h^2\boldsymbol{k}_i^T\boldsymbol{E}\boldsymbol{k}_i\mathrm{d}\Omega_{i,0}, \tag{29}$$

where $\boldsymbol{E}$ is the matrices of elastic coefficients for the plane-stress conditions [26],

$$\boldsymbol{E}=\frac{E}{1-\nu^2}\begin{bmatrix}1 & \nu & 0\\ \nu & 1 & 0\\ 0 & 0 & (1-\nu)/2\end{bmatrix}, \tag{30}$$

where h is the thickness of facet.

Similar to derivation of equation (25), the strain energy of facet elements can be further rewritten as

$$U=\sum_{i=1}^{m}\frac{1}{2}\int_{\mathrm{A}_i}\boldsymbol{\varepsilon}_i^T\boldsymbol{E}\boldsymbol{\varepsilon}_i\left|\mathbf{J}\right|\mathrm{dA}_i+\frac{1}{2}\int_{\mathrm{A}_i}h^2\boldsymbol{k}_i^T\boldsymbol{E}\boldsymbol{k}_i\left|\mathbf{J}\right|\mathrm{dA}_i. \tag{31}$$

The strain energy in equation (31) consists of two components. The first one comes from the longitudinal and shear deformations in the midplane, and the second one comes from bending and twisting. The nonlinear Green–Lagrange strain measure is used to account for all geometric nonlinearity, and to ensure zero strain under rigid body motions [27]. For the plane stress conditions, the stresses in the plate thickness direction are assumed to be zero and the strains in this direction are expressed as a function of the strains at the element mid-surface. The strain vector $\boldsymbol{\varepsilon}_i$ at the mid-surface of element. i .is [28]

$$\boldsymbol{\varepsilon}_i=[\varepsilon_{11}\quad\varepsilon_{22}\quad 2\varepsilon_{12}]^T,\qquad \varepsilon_{ij}=\frac{1}{2}(\mathbf{r}_{X_i}^T\mathbf{r}_{X_j}-\delta_{ij}). \tag{32}$$

The first derivatives of the global position vector with respect to global coordinates can be further derived from the definition of deformation gradient in Section 3.1.2 as,

$$\begin{aligned}\mathbf{r}_{X_i}&=\frac{\partial\mathbf{r}}{\partial X_i}=\frac{\partial(\mathbf{Se})}{\partial X_i}=\frac{\partial\mathbf{S}}{\partial X_i}\mathbf{e}=\frac{\partial\mathbf{S}}{\partial\chi_j}\frac{\partial\chi_j}{\partial X_i}\mathbf{e}={}_{ij}(\mathbf{J}^T)^{-1}\mathbf{S}_j\mathbf{e}\\&={}_i\mathbf{Se},\end{aligned} \tag{33}$$

where ${}_{ij}(\mathbf{J}^T)^{-1}$ denotes the component of $(\mathbf{J}^T)^{-1}$ at its i^{th} row and j^{th} column; $\mathbf{S}_j$ denotes the first derivatives of shape function matrix with respect to the independent iso-parametric coordinates; and ${}_i\mathbf{S}={}_{ij}(\mathbf{J}^T)^{-1}\mathbf{S}_j$.

In order to calculate the bending and twisting deformation of the facet elements, the curvature $\boldsymbol{k}_i$ at the mid-surface of element i is defined as [25]

$$\boldsymbol{k}_i=[k_{11}\quad k_{22}\quad 2k_{12}]^{\mathrm{T}},\qquad k_{ij}\approx\frac{\mathbf{r}_{ij}^T\mathbf{N}}{\left\|\mathbf{N}\right\|}, \tag{34}$$

where $\mathbf{N}$ is the normal vector of the element mid-surface, and it can be calculated as $\mathbf{n}=\mathbf{r}_i\times\mathbf{r}_j$. Here, the first and second derivatives of the global position vector with respect to the independent iso-parametric coordinates in Section 3.1.1 can be written as

$$\mathbf{r}_i=\frac{\partial\mathbf{r}}{\partial\chi_i}=\frac{\partial(\mathbf{Se})}{\partial\chi_i}=\frac{\partial\mathbf{S}}{\partial\chi_i}\mathbf{e}=\mathbf{S}_i\mathbf{e}, \tag{35}$$

$$\mathbf{r}_{ij}=\frac{\partial\mathbf{r}}{\partial\chi_i\chi_j}=\frac{\partial(\mathbf{Se})}{\partial\chi_i\chi_j}=\frac{\partial\mathbf{S}}{\partial\chi_i\chi_j}\mathbf{e}=\mathbf{S}_{ij}\mathbf{e}, \tag{36}$$

where $\mathbf{S}_{ij}$ denotes the second derivatives of shape function matrix with respect to independent iso-parametric coordinates.

The elemental internal force vector can be calculated using the strain energy as follows

$$\mathbf{Q}_e=\frac{\partial U}{\partial\mathbf{e}}=\sum_{i=1}^{m}\int_{\mathrm{A}_i}(\frac{\partial\boldsymbol{\varepsilon}_i}{\partial\mathbf{e}})^T\boldsymbol{E}_e\boldsymbol{\varepsilon}_i\left|\mathbf{J}\right|\mathrm{dA}_i+\int_{\mathrm{A}_i}(\frac{\partial\boldsymbol{k}_i}{\partial\mathbf{e}})^T\boldsymbol{E}_k\boldsymbol{k}_i\left|\mathbf{J}\right|\mathrm{dA}_i. \tag{37}$$

Here, the gradients of strains can be written as

$$(\frac{\partial\boldsymbol{\varepsilon}_i}{\partial\mathbf{e}})^{\mathrm{T}}=\begin{bmatrix}\frac{\partial\varepsilon_{11}}{\partial\mathbf{e}} & \frac{\partial\varepsilon_{22}}{\partial\mathbf{e}} & \frac{\partial\varepsilon_{12}}{\partial\mathbf{e}}\end{bmatrix}, \tag{38}$$

$$\begin{aligned}\frac{\partial\varepsilon_{ij}}{\partial\mathbf{e}}&=\frac{\partial(\frac{1}{2}(\mathbf{r}_{X_i}^{\mathrm{T}}\mathbf{r}_{X_j}-\delta_{ij}))}{\partial\mathbf{e}}=\frac{1}{2}\frac{\partial(\mathbf{r}_{X_i}^{\mathrm{T}}\mathbf{r}_{X_j})}{\partial\mathbf{e}}\\&=\frac{1}{2}\left[\mathbf{r}_{X_i}^{\mathrm{T}}\frac{\partial(\mathbf{r}_{X_j})}{\partial\mathbf{e}}+\mathbf{r}_{X_j}^{\mathrm{T}}\frac{\partial(\mathbf{r}_{X_i})}{\partial\mathbf{e}}\right]\\&=\frac{1}{2}\left[({}_i\mathbf{Se})^{\mathrm{T}}\frac{\partial({}_j\mathbf{Se})}{\partial\mathbf{e}}+({}_i\mathbf{Se})^{\mathrm{T}}\frac{\partial({}_i\mathbf{Se})}{\partial\mathbf{e}}\right]\\&=\mathbf{e}^T\left[\frac{1}{2}({}_i\mathbf{S}^{\mathrm{T}}{}_j\mathbf{S}+{}_j\mathbf{S}^{\mathrm{T}}{}_i\mathbf{S})\right]=\mathbf{e}^{\mathrm{T}}\mathbf{S}_{ij}^{\varepsilon}.\end{aligned} \tag{39}$$

where $\mathbf{S}_{ij}^{\varepsilon}=\frac{1}{2}({}_i\mathbf{S}^{\mathrm{T}}{}_j\mathbf{S}+{}_j\mathbf{S}^{\mathrm{T}}{}_i\mathbf{S})$.

Similarly, the gradients of curvatures are

$$(\frac{\partial\boldsymbol{k}_i}{\partial\mathbf{e}})^{\mathrm{T}}=\begin{bmatrix}\frac{\partial k_{11}}{\partial\mathbf{e}} & \frac{\partial k_{22}}{\partial\mathbf{e}} & \frac{\partial k_{12}}{\partial\mathbf{e}}\end{bmatrix}, \tag{40}$$

$$\frac{\partial k_{ij}}{\partial\mathbf{e}}\approx\frac{\partial(\frac{\mathbf{r}_{ij}^T\mathbf{N}}{\left\|\mathbf{N}\right\|})}{\partial\mathbf{e}}=\frac{1}{f}\left(\mathbf{r}_{ij}^T\frac{\partial\mathbf{N}}{\partial\mathbf{e}}+\mathbf{N}^T\frac{\partial\mathbf{r}_{ij}}{\partial\mathbf{e}}\right)-\frac{1}{f^2}\frac{\partial f}{\partial\mathbf{e}}\left(\mathbf{r}_{ij}^T\mathbf{N}\right), \tag{41}$$

where $f = \|\mathbf{N}\| = \sqrt{\mathbf{N}^T\mathbf{N}}$. In the case of stiff material, the last component of equation (41) is small compared with the first one so it can be neglected. Moreover,

$$\frac{\partial \mathbf{N}}{\partial \mathbf{e}} = \frac{\partial(\mathbf{r}_i \times \mathbf{r}_j)}{\partial \mathbf{e}} = \frac{\partial \mathbf{r}_i}{\partial \mathbf{e}} \times \mathbf{r}_j + \mathbf{r}_i \times \frac{\partial \mathbf{r}_j}{\partial \mathbf{e}} = \frac{\partial(\mathbf{S}_i\mathbf{e})}{\partial \mathbf{e}} \times (\mathbf{S}_j\mathbf{e}) + (\mathbf{S}_i\mathbf{e}) \times \frac{\partial(\mathbf{S}_j\mathbf{e})}{\partial \mathbf{e}} = \mathbf{S}_i \times (\mathbf{S}_j\mathbf{e}) + (\mathbf{S}_i\mathbf{e}) \times \mathbf{S}_j. \tag{42}$$

Hence

$$\frac{\partial k_{ij}}{\partial \mathbf{e}} \approx \frac{1}{f}\left[(\mathbf{S}_{ij}\mathbf{e})^T \frac{\partial \mathbf{N}}{\partial \mathbf{e}} + \mathbf{N}^T \frac{\partial(\mathbf{S}_{ij}\mathbf{e})}{\partial \mathbf{e}} \right] = \frac{1}{f}\left[\mathbf{e}^T\mathbf{S}_{ij}^T(\mathbf{S}_i \times (\mathbf{S}_j\mathbf{e}) + (\mathbf{S}_i\mathbf{e}) \times \mathbf{S}_j) + \mathbf{N}^T\mathbf{S}_{ij} \right]. \tag{43}$$

The tangent stiffness matrix of the facet elements can be furtherly calculated as [18]

$$\mathbf{K}_e = \frac{\partial \mathbf{Q}_e}{\partial \mathbf{e}} = \sum_{i=1}^{m} \int_{A_i} (\frac{\partial \boldsymbol{\varepsilon}_i}{\partial \mathbf{e}})^T \boldsymbol{E}_\varepsilon (\frac{\partial \boldsymbol{\varepsilon}_i}{\partial \mathbf{e}}) |\mathbf{J}| \mathrm{d}A_i ... + \int_{A_i} (\frac{\partial \boldsymbol{k}_i}{\partial \mathbf{e}})^T \boldsymbol{E}_k (\frac{\partial \boldsymbol{k}_i}{\partial \mathbf{e}}) |\mathbf{J}| \mathrm{d}A_i. \tag{44}$$

3.3.3 Creases folding energy

The definition of the folding energy of creases are discussed earlier in Section 3.2. Here, the internal force vector and tangent stiffness matrix of creases are provided by calculating from the folding energy of creases.

The folding energy of creases is defined as

$$U_f = \sum_{j=1}^{n}\sum_{j=1}^{l} U_{f,j} = \sum_{j=1}^{n}\sum_{j=1}^{l} \frac{1}{2} k_f \left(\theta_j - \theta_{j,0}\right)^2 \tag{45}$$

where n is the number of creases. $U_{f,j}$ denotes the folding energy of the j^{th} rotational spring.

Take the rotational spring at node 1 in Figure 5 as an example, the internal force vector can be calculated as

$$\mathbf{Q}_{f,1} = \frac{\partial U_{f,1}}{\partial \mathbf{e}} = k_f \left(\theta_1 - \theta_{1,0}\right) \frac{\partial \theta_1}{\partial \mathbf{e}} \tag{46}$$

Here, the first derivative (aka, gradients) of folding angle θ_1 with respect to nodal coordinates can be summarized as

$$\frac{\partial \theta_1}{\partial \mathbf{r}_{\eta_i}^{\mathrm{I1}}} = \frac{\left\|\boldsymbol{r}_{\zeta_i}^{\mathrm{I1}}\right\|}{\|\boldsymbol{m}\|^2}\boldsymbol{m}, \tag{47}$$

$$\frac{\partial \theta_1}{\partial \mathbf{r}_{\zeta_i}^{\mathrm{III}}} = \frac{\left\|\mathbf{r}_{\eta_i}^{\mathrm{III}}\right\|}{\|\boldsymbol{n}\|^2}\boldsymbol{n}, \tag{48}$$

$$\frac{\partial \theta_1}{\partial \mathbf{r}_{\zeta_i}^{\mathrm{I1}}} = A\frac{\partial \theta_1}{\partial \mathbf{r}_{\zeta_i}^{\mathrm{III}}} - B\frac{\partial \theta_1}{\partial \mathbf{r}_{\eta_i}^{\mathrm{I1}}}, \tag{49}$$

where

$$A = \frac{\mathbf{r}_{\zeta_i}^{\mathrm{III}} \cdot \mathbf{r}_{\eta_i}^{\mathrm{III}}}{\left\|\mathbf{r}_{\eta_i}^{\mathrm{III}}\right\|^2} \quad \text{and} \quad B = \frac{\mathbf{r}_{\eta_i}^{\mathrm{I1}} \cdot \mathbf{r}_{\zeta_i}^{\mathrm{I1}}}{\left\|\mathbf{r}_{\zeta_i}^{\mathrm{I1}}\right\|^2} \tag{50}$$

All other first derivatives of the folding angle θ_1 with respect to nodal coordinates are $\mathbf{0}$, since θ_1 is function of $\mathbf{r}_{\eta_i}^{\mathrm{I1}}$, $\mathbf{r}_{\zeta_i}^{\mathrm{I1}}$, and $\mathbf{r}_{\zeta_i}^{\mathrm{III}}$, as shown in equation (16) and (17). More details of the derivation of gradients of folding angle are elaborated in Appendix B.

The tangent stiffness matrix can be further calculated as

$$\mathbf{K}_{f,1} = \frac{\partial \mathbf{Q}_{f,1}}{\partial \mathbf{e}} = k_f \frac{\partial \theta_1}{\partial \mathbf{e}} \otimes \frac{\partial \theta_1}{\partial \mathbf{e}} + k_f \left(\theta_1 - \theta_{1,0}\right) \frac{\partial^2 \theta_1}{\partial^2 \mathbf{e}} \tag{51}$$

The complete Hessian matrix (the second-order derivative of the folding angle with respect to nodal coordinates) has 9 blocks of submatrices, where each block is of size 3 by 3. Owing to symmetry of the Hessian matrix, we only need to derive 6 blocks of such submatrices. For example, the first block, i.e. the derivative with respect to the position gradient vector $\mathbf{r}_{\eta_i}^{\mathrm{I1}}$ at node 1, is given by

$$\frac{\partial^2 \theta_1}{\partial (\mathbf{r}_{\eta_i}^{\mathrm{I1}})^2} = -\frac{\left\|\boldsymbol{r}_{\zeta_i}^{\mathrm{I1}}\right\|}{\|\boldsymbol{m}\|^4}\left[\boldsymbol{m} \otimes (\boldsymbol{r}_{\zeta_i}^{\mathrm{I1}} \times \boldsymbol{m}) + (\boldsymbol{r}_{\zeta_i}^{\mathrm{I1}} \times \boldsymbol{m}) \otimes \boldsymbol{m}\right], \tag{52}$$

The operator ' $\otimes$ ' between two vectors is the tensor product. More details of the derivation of Hessian matrix are elaborated in Appendix C.

Therefore, the internal force vector and tangent stiffness matrix of rotational springs can be calculated as

$$\mathbf{Q}_f = \sum_{j=1}^{n}\sum_{j=1}^{l} \mathbf{Q}_{f,j} \tag{53}$$

$$\mathbf{K}_f = \sum_{j=1}^{n}\sum_{j=1}^{l} \mathbf{K}_{f,j} \tag{54}$$

3.3.4 Kinetic energy

In the iso-ANCF method, the mass matrix of the plate element can be obtained using the following expression [17]

$$T = \sum_{i=1}^{m} \frac{1}{2} \int_{\Omega_i} \rho \dot{\mathbf{r}}_i^{\mathrm{T}} \dot{\mathbf{r}}_i \mathrm{d}\Omega_i . \tag{55}$$

where $\dot{\mathbf{r}}_i$ is the absolute velocity vector of facet element *i*, and it can be written as

$$\dot{\mathbf{r}} = \mathbf{S}\dot{\mathbf{e}}. \tag{56}$$

Similar to the derivation of equation (25), the kinetic energy of facet elements can be rewritten as

$$T = \sum_{i=1}^{m} \frac{1}{2} \int_{\mathrm{A}_i} \rho_0 \dot{\mathbf{r}}_i^{\mathrm{T}} \dot{\mathbf{r}}_i \left|\mathbf{J}\right| \mathrm{dA}_i , \tag{57}$$

where ρ and ρ_0 are the mass density in current configuration and initial configuration, respectively. Here, $\rho \mathrm{d}\Omega_i = \rho_0 \mathrm{d}\Omega_{i,0}$ is applied.

Hence,

$$T = \sum_{i=1}^{m} \frac{1}{2} \int_{\mathrm{A}_i} \rho_0 (\mathbf{S}\dot{\mathbf{e}}_i)^{\mathrm{T}} (\mathbf{S}\dot{\mathbf{e}}_i) \left|\mathbf{J}\right| \mathrm{dA}_i = \frac{1}{2} \dot{\mathbf{e}}^T \mathbf{M} \dot{\mathbf{e}}, \tag{58}$$

where the mass matrix is

$$\mathbf{M} = \sum_{i=1}^{m} \mathbf{M}_i = \sum_{i=1}^{m} \int_{\mathrm{A}_i} \rho_0 \mathbf{S}^T \mathbf{S} \left|\mathbf{J}\right| \mathrm{dA}_i \tag{59}$$

3.4 Final Solution

In summary, by substituting equations (28), (37), (53) and (58) into equation (21), one can update the dynamic equations of motion for origami folding as

$$\mathbf{M}\ddot{\mathbf{e}} + \mathbf{Q}_e + \mathbf{Q}_f = \mathbf{Q}_g . \tag{60}$$

Or it can be written as

$$\mathbf{M}\ddot{\mathbf{e}} + \mathbf{K}_e \mathbf{e} + \mathbf{K}_f \mathbf{e} = \mathbf{Q}_g . \tag{61}$$

The noncommercial multibody and finite element research code HOTINT is used for solving (60) or (61).

4. CONCLUSION

This paper presents a new high-fidelity dynamic model for origami folding based on the iso−parametric Absolute Nodal Coordinate Formulation (iso-ANCF). The iso-ANCF uses position and position gradients instead of displacement and rotation as the nodal coordinates, so it is efficient and robust for the large deformation and rotation analysis of origami folding. In the context of iso-ANCF method, this study develops a new crease model by treating them as rotational springs at the crease nodes. The corresponding folding angle is defined based on the local surface normal vectors at the crease nodes. Besides, based on the proposed model, this paper formulates a new tangent stiffness matrix of the creases and provides the final equations of motion for origami folding. Compared to the currently popular origami mechanics models like the nonlinear bar-hinge model [11], this new model is more advanced in that its definition of folding angle θ is valid for complex origami structures with curved crease pattern. Besides, it is more consitent with the actural origami structures by using continuous shell elements instead of 1-D bar element. Compared to the traditional finite element method, the iso-ANCF methodallows complex origami structures to be simulated using a smaller number of elements. Moreover, the dynamic analysis of origami subjected to large deformation and rotations is more computationally efficient due to the use of global position gradients and shape functions

ACKNOWLEDGEMENT

The authors acknowledge the partial support from the National Science Foundation (Award # CMMI-1633952, 1751449 CA-REER) and Clemson University (via startup funding and the CECAS Dean's Faculty Fellow Award), the China Scholarship Council (CSC).

REFERENCES

[1] Fang, H., Li, S., Ji, H., & Wang, K. W. (2017). Dynamics of a bistable Miura-origami structure. Physical Review E, 95(5), 052211.

[2] Sengupta, S., & Li, S. (2018). Harnessing the anisotropic multistability of stacked-origami mechanical metamaterials for effective modulus programming. Journal of Intelligent Material Systems and Structures, 29(14), 2933-2945.

[3] Li, S., Fang, H., Sadeghi, S., Bhovad, P., & Wang, K. W. (2018). Architected Origami Materials: How Folding Creates Sophisticated Mechanical Properties. Advanced Materials, 1805282.

[4] Gattas, J. M., Wu, W., & You, Z. (2013). Miura-base rigid origami: parameterizations of first-level derivative and piecewise geometries. Journal of Mechanical design, 135(11), 111011.

[5] Zhou, X., Zang, S., & You, Z. (2016). Origami mechanical metamaterials based on the Miura-derivative fold patterns. Proceedings of the Royal Society A: Mathematical, Physical and Engineering Sciences, 472(2191), 20160361.

[6] Resch, R. (1970). The design and analysis of kinematic folded plate systems. In Proceedings of IASS Symposium on Folded Plates and Prismatic Structures, 1970.

[7] Schenk M. 2011 Folded shell structures [Clare College]. Cambridge, UK: University of Cambridge.

[8] Li, S., & Wang, K. W. (2015). Fluidic origami: a plant-inspired adaptive structure with shape morphing and stiffness tuning. Smart Materials and Structures, 24(10),

105031.
[9] Silverberg, J. L., Evans, A. A., McLeod, L., Hayward, R. C., Hull, T., Santangelo, C. D., & Cohen, I. (2014). Using origami design principles to fold reprogrammable mechanical metamaterials. science, 345(6197), 647-650.
[10] Schenk, M., & Guest, S. D. (2011, March). Origami folding: A structural engineering approach. In Origami 5: Fifth International Meeting of Origami Science, Mathematics, and Education (pp. 291-304). CRC Press, Boca Raton, FL.
[11] Liu, K., & Paulino, G. H. (2017). Nonlinear mechanics of non-rigid origami: an efficient computational approach. Proceedings of the Royal Society A: Mathematical, Physical and Engineering Sciences, 473(2206), 20170348.
[12] Gillman, A., Fuchi, K., & Buskohl, P. R. (2018). Truss-based nonlinear mechanical analysis for origami structures exhibiting bifurcation and limit point instabilities. International Journal of Solids and Structures, 147, 80-93.
[13] Li, S., Fang, H., Sadeghi, S., Bhovad, P., & Wang, K. W. (2018). Architected Origami Materials: How Folding Creates Sophisticated Mechanical Properties. Advanced Materials, 1805282.
[14] Zhou, X., Zang, S., & You, Z. (2016). Origami mechanical metamaterials based on the Miura-derivative fold patterns. Proceedings of the Royal Society A: Mathematical, Physical and Engineering Sciences, 472(2191), 20160361.
[15] Filipov, E. T., Tachi, T., & Paulino, G. H. (2015). Origami tubes assembled into stiff, yet reconfigurable structures and metamaterials. Proceedings of the National Academy of Sciences, 112(40), 12321-12326.
[16] Fischer, S. (2015). Realistic Fe simulation of foldcore sandwich structures. International Journal of Mechanical and Materials Engineering, 10(1), 14.
[17] Mikkola, A. M., & Shabana, A. A. (2003). A non-incremental finite element procedure for the analysis of large deformation of plates and shells in mechanical system applications. Multibody System Dynamics, 9(3), 283-309.
[18] Vaziri Sereshk, M., & Salimi, M. (2011). Comparison of finite element method based on nodal displacement and absolute nodal coordinate formulation (ANCF) in thin shell analysis. International Journal for Numerical Methods in Biomedical Engineering, 27(8), 1185-1198.
[19] Shabana, A. A. (1998). Computer implementation of the absolute nodal coordinate formulation for flexible multibody dynamics. Nonlinear Dynamics, 16(3), 293-306.
[20] Yakoub, R. Y., & Shabana, A. A. (1999). Use of Cholesky coordinates and the absolute nodal coordinate formulation in the computer simulation of flexible multibody systems. Nonlinear Dynamics, 20(3), 267-282.
[21] Pappalardo, C. M., Wang, T., & Shabana, A. A. (2017). On the formulation of the planar ANCF triangular finite elements. Nonlinear Dynamics, 89(2), 1019-1045.
[22] Bonet, J., Gil, A. J., & Wood, R. D. (2016). Nonlinear solid mechanics for finite element analysis: statics. Cambridge University Press.
[23] Rojas, S., Boston, D. M., & Arrieta, A. F. (2019, March). Actuation simplification for grippers based on bioinspired spring origami. In Bioinspiration, Biomimetics, and Bioreplication IX (Vol. 10965, p. 109650O). International Society for Optics and Photonics.
[24] Dmitrochenko, O. N., & Pogorelov, D. Y. (2003). Generalization of plate finite elements for absolute nodal coordinate formulation. Multibody System Dynamics, 10(1), 17-43.
[25] Filipov, E. T., Liu, K., Tachi, T., Schenk, M., & Paulino, G. H. (2017). Bar and hinge models for scalable analysis of origami. International Journal of Solids and Structures, 124, 26-45.
[26] Schwab, A. L., Gerstmayr, J., & Meijaard, J. P. (2007, January). Comparison of three-dimensional flexible thin plate elements for multibody dynamic analysis: finite element formulation and absolute nodal coordinate formulation. In ASME 2007 International Design Engineering Technical Conferences and Computers and Information in Engineering Conference (pp. 1059-1070). American Society of Mechanical Engineers.
[27] Dufva, K., & Shabana, A. A. (2005). Use of the absolute nodal coordinate formulation in the analysis of thin plate structures. Techn. Rep. No. MBS05–1-UIC, Univ. of Illinois at Chicago, Chicago IL.
[28] Dufva, K., & Shabana, A. A. (2005). Analysis of thin plate structures using the absolute nodal coordinate formulation. Proceedings of the Institution of Mechanical Engineers, Part K: Journal of Multi-body Dynamics, 219(4), 345-355.
[29] Kikuchi, N. (1986). Finite element methods in mechanics. CUP Archive.

APPENDIX

APPENDIX A: SHAPE FUNCTIONS OF ISO-ANCF ELEMENT

The shape functions of the iso-ANCF element introduced in (5) is

$$s_1 = \xi\left(\xi^2 + 3\xi(\eta+\zeta) + 2\eta\zeta\right) \tag{62}$$

$$s_2 = \frac{1}{3}\xi\eta(3\xi - \zeta) \tag{63}$$

$$s_3 = \frac{1}{3}\xi\zeta(3\xi - \eta) \tag{64}$$

$$s_4 = \eta\left(\eta^2 + 3\eta(\zeta+\xi) + 2\zeta\xi\right) \tag{65}$$

$$s_5 = \frac{1}{3}\eta\zeta(3\eta - \xi) \tag{66}$$

$$s_6 = \frac{1}{3}\eta\xi(3\eta - \zeta) \tag{67}$$

$$s_7 = \zeta\left(\zeta^2 + 3\zeta(\xi + \eta) + 2\xi\eta\right) \tag{68}$$

$$s_8 = \frac{1}{3}\zeta\eta(3\zeta - \eta) \tag{69}$$

$$s_9 = \frac{1}{3}\zeta\eta(3\zeta - \xi) \tag{70}$$

where ξ , η , ζ ,are the independent isoparametric coordinates. Here subscript i is omitted for notation convenience [21].

APPENDIX B: GRADIENTS OF FOLDING ANGLE

The derivation of gradients of folding angle θ_1 at node 1 is shown in follows.

$$\begin{aligned}
\frac{\partial\theta_1}{\partial\mathbf{r}_{\eta_i}^{\mathrm{II}1}} &= \frac{\partial(\eta\arccos\left(\dfrac{\boldsymbol{m}\cdot\boldsymbol{n}}{\|\boldsymbol{m}\|\cdot\|\boldsymbol{n}\|}\right))}{\partial\mathbf{r}_{\eta_i}^{\mathrm{II}1}} \\
&= \frac{-1}{\sin\theta_1}\frac{\|\boldsymbol{m}\|\|\boldsymbol{n}\|\dfrac{\partial(\boldsymbol{m}\cdot\boldsymbol{n})}{\partial\mathbf{r}_{\eta_i}^{\mathrm{II}1}} - (\boldsymbol{m}\cdot\boldsymbol{n})\dfrac{\partial(\|\boldsymbol{m}\|\cdot\|\boldsymbol{n}\|)}{\partial\mathbf{r}_{\eta_i}^{\mathrm{II}1}}}{\left(\|\boldsymbol{m}\|\cdot\|\boldsymbol{n}\|\right)^2} \\
&= \frac{-1}{\sin\theta_1}\left[\frac{1}{\|\boldsymbol{m}\|\|\boldsymbol{n}\|}\left(\boldsymbol{m}^T\frac{\partial\boldsymbol{n}}{\partial\mathbf{r}_{\eta_i}^{\mathrm{II}1}} + \boldsymbol{n}^T\frac{\partial\boldsymbol{m}}{\partial\mathbf{r}_{\eta_i}^{\mathrm{II}1}}\right) - \frac{(\boldsymbol{m}\cdot\boldsymbol{n})\left(\|\boldsymbol{m}\|\dfrac{\partial(\|\boldsymbol{n}\|)}{\partial\mathbf{r}_{\eta_i}^{\mathrm{II}1}} + \|\boldsymbol{n}\|\dfrac{\partial(\|\boldsymbol{m}\|)}{\partial\mathbf{r}_{\eta_i}^{\mathrm{II}1}}\right)}{\left(\|\boldsymbol{m}\|\cdot\|\boldsymbol{n}\|\right)^2}\right] \\
&= \frac{-1}{\sin\theta_1}\left[\frac{1}{\|\boldsymbol{m}\|\|\boldsymbol{n}\|}\left(\boldsymbol{n}^T\frac{\partial\left(\mathbf{r}_{\eta_i}^{\mathrm{II}1}\times\mathbf{r}_{\zeta_i}^{\mathrm{II}1}\right)}{\partial\mathbf{r}_{\eta_i}^{\mathrm{II}1}}\right) - \frac{(\boldsymbol{m}\cdot\boldsymbol{n})\left(\|\boldsymbol{n}\|\dfrac{\partial((\boldsymbol{m}\cdot\boldsymbol{m})^{\frac{1}{2}})}{\partial\mathbf{r}_{\eta_i}^{\mathrm{II}1}}\right)}{\left(\|\boldsymbol{m}\|\cdot\|\boldsymbol{n}\|\right)^2}\right] \\
&= \frac{-1}{\sin\theta_1}\left[\frac{\boldsymbol{n}^T}{\|\boldsymbol{m}\|\|\boldsymbol{n}\|}\left(\mathbf{I}\times\mathbf{r}_{\zeta_i}^{\mathrm{II}1}\right) - \frac{(\boldsymbol{m}\cdot\boldsymbol{n})\|\boldsymbol{n}\|\boldsymbol{m}^T}{\left(\|\boldsymbol{m}\|\cdot\|\boldsymbol{n}\|\right)^2\|\boldsymbol{m}\|}\frac{\partial\boldsymbol{m}}{\partial\mathbf{r}_{\eta_i}^{\mathrm{II}1}}\right] \\
&= \frac{-1}{\sin\theta_1}\frac{\|\boldsymbol{m}\|^2\boldsymbol{n}\cdot\left(\mathbf{I}\times\mathbf{r}_{\zeta_i}^{\mathrm{II}1}\right) - (\boldsymbol{m}\cdot\boldsymbol{n})\boldsymbol{m}\cdot\left(\mathbf{I}\times\mathbf{r}_{\zeta_i}^{\mathrm{II}1}\right)}{\|\boldsymbol{m}\|^3\cdot\|\boldsymbol{n}\|} \\
&= \frac{-1}{\sin\theta_1}\mathbf{r}_{\zeta_i}^{\mathrm{II}1}\times\frac{\|\boldsymbol{m}\|^2\boldsymbol{n} - (\boldsymbol{m}\cdot\boldsymbol{n})\boldsymbol{m}}{\|\boldsymbol{m}\|^3\cdot\|\boldsymbol{n}\|}
\end{aligned} \tag{71}$$

The expressions contain terms that will reach singularity when $\sin\theta_1 = 0$. Based on research work done by Liu et al. [11], one can obtain equivalent expressions for the gradients that are free of any singularities, that is

$$\begin{aligned}
\frac{\partial\theta_1}{\partial\mathbf{r}_{\eta_i}^{\mathrm{II}1}} &= \frac{-1}{\sin\theta_1}\mathbf{r}_{\zeta_i}^{\mathrm{II}1}\times\frac{\|\boldsymbol{m}\|^2\boldsymbol{n} - (\boldsymbol{m}\cdot\boldsymbol{n})\boldsymbol{m}}{\|\boldsymbol{m}\|^3\cdot\|\boldsymbol{n}\|} \\
&= \frac{-1}{\sin\theta_1}\mathbf{r}_{\zeta_i}^{\mathrm{II}1}\times\frac{\boldsymbol{m}\times(\boldsymbol{n}\times\boldsymbol{m})}{\|\boldsymbol{m}\|^3\cdot\|\boldsymbol{n}\|} \\
&= \frac{-1}{\sin\theta_1}\mathbf{r}_{\zeta_i}^{\mathrm{II}1}\times\frac{-\boldsymbol{m}\times\left(\|\boldsymbol{m}\|\|\boldsymbol{n}\|\sin\theta_1\mathbf{r}_{\zeta_i}^{\mathrm{II}1}\right)}{\left\|\mathbf{r}_{\zeta_i}^{\mathrm{II}1}\right\|\|\boldsymbol{m}\|^3\cdot\|\boldsymbol{n}\|} \\
&= \frac{\mathbf{r}_{\zeta_i}^{\mathrm{II}1}\times\boldsymbol{m}\times\mathbf{r}_{\zeta_i}^{\mathrm{II}1}}{\left\|\mathbf{r}_{\zeta_i}^{\mathrm{II}1}\right\|\|\boldsymbol{m}\|^2} \\
&= \frac{\left\|\mathbf{r}_{\zeta_i}^{\mathrm{II}1}\right\|}{\|\boldsymbol{m}\|^2}\boldsymbol{m}
\end{aligned} \tag{72}$$

Following the same procedure, one can obtain

$$\frac{\partial\theta}{\partial\mathbf{r}_{\zeta_i}^{\mathrm{III}1}} = \frac{\left\|\mathbf{r}_{\eta_i}^{\mathrm{III}1}\right\|}{\|\boldsymbol{n}\|^2}\boldsymbol{n} \tag{73}$$

And,

$$\begin{aligned}
\frac{\partial\theta_1}{\partial\mathbf{r}_{\zeta_i}^{\mathrm{II}1}} &= \frac{\partial(\eta\arccos\left(\dfrac{\boldsymbol{m}\cdot\boldsymbol{n}}{\|\boldsymbol{m}\|\cdot\|\boldsymbol{n}\|}\right))}{\partial\mathbf{r}_{\zeta_i}^{\mathrm{II}1}} \\
&= \frac{-1}{\sin\theta_1}\frac{\|\boldsymbol{m}\|\|\boldsymbol{n}\|\dfrac{\partial(\boldsymbol{m}\cdot\boldsymbol{n})}{\partial\mathbf{r}_{\zeta_i}^{\mathrm{II}1}} - (\boldsymbol{m}\cdot\boldsymbol{n})\dfrac{\partial(\|\boldsymbol{m}\|\cdot\|\boldsymbol{n}\|)}{\partial\mathbf{r}_{\zeta_i}^{\mathrm{II}1}}}{\left(\|\boldsymbol{m}\|\cdot\|\boldsymbol{n}\|\right)^2} \\
&= \frac{-1}{\sin\theta_1}\left[\frac{1}{\|\boldsymbol{m}\|\|\boldsymbol{n}\|}\left(\boldsymbol{m}^T\frac{\partial\boldsymbol{n}}{\partial\mathbf{r}_{\zeta_i}^{\mathrm{II}1}} + \boldsymbol{n}^T\frac{\partial\boldsymbol{m}}{\partial\mathbf{r}_{\zeta_i}^{\mathrm{II}1}}\right) - \frac{(\boldsymbol{m}\cdot\boldsymbol{n})\left(\|\boldsymbol{m}\|\dfrac{\partial(\|\boldsymbol{n}\|)}{\partial\mathbf{r}_{\zeta_i}^{\mathrm{II}1}} + \|\boldsymbol{n}\|\dfrac{\partial(\|\boldsymbol{m}\|)}{\partial\mathbf{r}_{\zeta_i}^{\mathrm{II}1}}\right)}{\left(\|\boldsymbol{m}\|\cdot\|\boldsymbol{n}\|\right)^2}\right] \\
&= \frac{-1}{\sin\theta_1}\left[\frac{1}{\|\boldsymbol{m}\|\|\boldsymbol{n}\|}\left(\boldsymbol{m}\times\mathbf{r}_{\zeta_i}^{\mathrm{III}1} + \boldsymbol{n}\times\mathbf{r}_{\eta_i}^{\mathrm{II}1}\right) - \frac{(\boldsymbol{m}\cdot\boldsymbol{n})\left(\|\boldsymbol{m}\|^2\boldsymbol{n}\times\mathbf{r}_{\zeta_i}^{\mathrm{III}1} + \|\boldsymbol{n}\|^2\boldsymbol{m}\times\mathbf{r}_{\eta_i}^{\mathrm{II}1}\right)}{\left(\|\boldsymbol{m}\|\cdot\|\boldsymbol{n}\|\right)^3}\right] \\
&= \frac{1}{\sin\theta_1}\frac{\left(\|\boldsymbol{m}\|\|\boldsymbol{n}\|\right)^2\left(\mathbf{r}_{\zeta_i}^{\mathrm{III}1}\times\boldsymbol{m} + \mathbf{r}_{\eta_i}^{\mathrm{I}4}\times\boldsymbol{n}\right) - (\boldsymbol{m}\cdot\boldsymbol{n})\left(\|\boldsymbol{m}\|^2\mathbf{r}_{\zeta_i}^{\mathrm{III}1}\times\boldsymbol{n} + \|\boldsymbol{n}\|^2\mathbf{r}_{\eta_i}^{\mathrm{II}1}\times\boldsymbol{m}\right)}{\left(\|\boldsymbol{m}\|\cdot\|\boldsymbol{n}\|\right)^3} \\
&= \frac{1}{\sin\theta_1}\mathbf{r}_{\zeta_i}^{\mathrm{III}1}\times\frac{\left(\|\boldsymbol{m}\|\|\boldsymbol{n}\|\right)^2\boldsymbol{m} - (\boldsymbol{m}\cdot\boldsymbol{n})\|\boldsymbol{m}\|^2\boldsymbol{n}}{\left(\|\boldsymbol{m}\|\cdot\|\boldsymbol{n}\|\right)^3} + \frac{1}{\sin\theta_1}\mathbf{r}_{\eta_i}^{\mathrm{II}1}\times\frac{\left(\|\boldsymbol{m}\|\|\boldsymbol{n}\|\right)^2\boldsymbol{n} - (\boldsymbol{m}\cdot\boldsymbol{n})\|\boldsymbol{n}\|^2\boldsymbol{m}}{\left(\|\boldsymbol{m}\|\cdot\|\boldsymbol{n}\|\right)^3} \\
&= \frac{1}{\sin\theta_1}\mathbf{r}_{\zeta_i}^{\mathrm{III}1}\times\frac{\|\boldsymbol{n}\|^2\boldsymbol{m} - (\boldsymbol{m}\cdot\boldsymbol{n})\boldsymbol{n}}{\|\boldsymbol{m}\|\|\boldsymbol{n}\|^3} + \frac{1}{\sin\theta_1}\mathbf{r}_{\eta_i}^{\mathrm{II}1}\times\frac{\|\boldsymbol{m}\|^2\boldsymbol{n} - (\boldsymbol{m}\cdot\boldsymbol{n})\boldsymbol{m}}{\|\boldsymbol{m}\|^3\|\boldsymbol{n}\|}
\end{aligned} \tag{74}$$

Based on research work done by Liu et al. [11], one can obtain

$$\begin{aligned}
\frac{\partial\theta_1}{\partial\mathbf{r}_{\zeta_i}^{\mathrm{II}1}} &= \frac{1}{\sin\theta_1}\mathbf{r}_{\zeta_i}^{\mathrm{III}1}\times\frac{\|\boldsymbol{n}\|^2\boldsymbol{m} - (\boldsymbol{m}\cdot\boldsymbol{n})\boldsymbol{n}}{\|\boldsymbol{m}\|\|\boldsymbol{n}\|^3} + \frac{1}{\sin\theta_1}\mathbf{r}_{\eta_i}^{\mathrm{II}1}\times\frac{\|\boldsymbol{m}\|^2\boldsymbol{n} - (\boldsymbol{m}\cdot\boldsymbol{n})\boldsymbol{m}}{\|\boldsymbol{m}\|^3\|\boldsymbol{n}\|} \\
&= \frac{1}{\sin\theta_1}\mathbf{r}_{\zeta_i}^{\mathrm{III}1}\times\frac{\boldsymbol{n}\times(\boldsymbol{m}\times\boldsymbol{n})}{\|\boldsymbol{n}\|^3\cdot\|\boldsymbol{m}\|} + \frac{1}{\sin\theta_1}\mathbf{r}_{\eta_i}^{\mathrm{II}1}\times\frac{\boldsymbol{m}\times(\boldsymbol{n}\times\boldsymbol{m})}{\|\boldsymbol{m}\|^3\cdot\|\boldsymbol{n}\|} \\
&= \frac{1}{\sin\theta_1}\mathbf{r}_{\zeta_i}^{\mathrm{III}1}\times\frac{\boldsymbol{n}\times\left(\|\boldsymbol{m}\|\|\boldsymbol{n}\|\sin\theta_1\mathbf{r}_{\eta_i}^{\mathrm{III}1}\right)}{\left\|\mathbf{r}_{\eta_i}^{\mathrm{III}1}\right\|\|\boldsymbol{n}\|^3\cdot\|\boldsymbol{m}\|} + \frac{1}{\sin\theta_1}\mathbf{r}_{\eta_i}^{\mathrm{II}1}\times\frac{-\boldsymbol{m}\times\left(\|\boldsymbol{m}\|\|\boldsymbol{n}\|\sin\theta_1\mathbf{r}_{\zeta_i}^{\mathrm{II}1}\right)}{\left\|\mathbf{r}_{\zeta_i}^{\mathrm{II}1}\right\|\|\boldsymbol{m}\|^3\cdot\|\boldsymbol{n}\|} \\
&= \frac{\mathbf{r}_{\zeta_i}^{\mathrm{III}1}\times\boldsymbol{n}\times\mathbf{r}_{\eta_i}^{\mathrm{III}1}}{\left\|\mathbf{r}_{\eta_i}^{\mathrm{III}1}\right\|\|\boldsymbol{n}\|^2} - \frac{\mathbf{r}_{\eta_i}^{\mathrm{II}1}\times\boldsymbol{m}\times\mathbf{r}_{\zeta_i}^{\mathrm{II}1}}{\left\|\mathbf{r}_{\zeta_i}^{\mathrm{I}4}\right\|\|\boldsymbol{m}\|^2} \\
&= \frac{\mathbf{r}_{\zeta_i}^{\mathrm{III}1}\cdot\mathbf{r}_{\eta_i}^{\mathrm{III}1}}{\left\|\mathbf{r}_{\eta_i}^{\mathrm{III}1}\right\|\|\boldsymbol{n}\|^2}\boldsymbol{n} - \frac{\mathbf{r}_{\eta_i}^{\mathrm{II}1}\cdot\mathbf{r}_{\zeta_i}^{\mathrm{II}1}}{\left\|\mathbf{r}_{\zeta_i}^{\mathrm{II}1}\right\|\|\boldsymbol{m}\|^2}\boldsymbol{m} \\
&= A\frac{\partial\theta_1}{\partial\mathbf{r}_{\zeta_i}^{\mathrm{III}1}} - B\frac{\partial\theta_1}{\partial\mathbf{r}_{\eta_i}^{\mathrm{II}1}}
\end{aligned} \tag{75}$$

where

$$A=\frac{\mathbf{r}_{\zeta_i}^{\mathrm{III}}\cdot\mathbf{r}_{\eta_i}^{\mathrm{III}}}{\left\|\mathbf{r}_{\eta_i}^{\mathrm{III}}\right\|^2}\quad\text{and}\quad B=\frac{\mathbf{r}_{\eta_i}^{\mathrm{II}}\cdot\mathbf{r}_{\zeta_i}^{\mathrm{II}}}{\left\|\mathbf{r}_{\zeta_i}^{\mathrm{II}}\right\|^2} \tag{76}$$

All other first derivatives of the folding angle θ with respect to nodal coordinates are $\mathbf{0}$, since θ_1 is function of $\mathbf{r}_{\eta_i}^{\mathrm{II}}$, $\mathbf{r}_{\zeta_i}^{\mathrm{II}}$, and $\mathbf{r}_{\zeta_i}^{\mathrm{III}}$, as shown in equation (16) and (17).

APPENDIX C: HESSIAN MATRIX OF FOLDING ANGLE

The Hessian matrix appears in the tangent stiffness matrices of rotational springs. The Hessian contains 9 blocks of submatrices (of size 3 × 3), among which there are 6 independent blocks due to symmetry.

Let us define a new operator ' $\odot$ ' as

$$\boldsymbol{a}\odot\boldsymbol{b}:=\boldsymbol{a}\otimes\boldsymbol{b}+\boldsymbol{b}\otimes\boldsymbol{a},\quad\forall\boldsymbol{a},\boldsymbol{b}\in R^3$$

Note that $\boldsymbol{a}\odot\boldsymbol{b}$ results in a symmetric matrix. The 6 independent blocks of the Hessian matrix of the rotation angle with respect to the nodal coordinates are expressed as

$$\frac{\partial^2\theta_1}{\partial(\mathbf{r}_{\eta_i}^{\mathrm{II}})^2}=-\frac{\left\|\boldsymbol{r}_{\zeta_i}^{\mathrm{II}}\right\|}{\|\boldsymbol{m}\|^4}\left[\boldsymbol{m}\odot(\boldsymbol{r}_{\zeta_i}^{\mathrm{II}}\times\boldsymbol{m})\right], \tag{77}$$

$$\frac{\partial^2\theta_1}{\partial(\mathbf{r}_{\zeta_i}^{\mathrm{III}})^2}=-\frac{\left\|\mathbf{r}_{\eta_i}^{\mathrm{III}}\right\|}{\|\boldsymbol{n}\|^4}\left[\boldsymbol{n}\odot(\mathbf{r}_{\eta_i}^{\mathrm{III}}\times\boldsymbol{n})\right], \tag{78}$$

$$\frac{\partial^2\theta_1}{\partial\mathbf{r}_{\eta_i}^{\mathrm{II}}\partial\mathbf{r}_{\zeta_i}^{\mathrm{II}}}=\frac{\boldsymbol{m}\otimes\boldsymbol{r}_{\zeta_i}^{\mathrm{II}}}{\|\boldsymbol{m}\|^2\left\|\boldsymbol{r}_{\zeta_i}^{\mathrm{II}}\right\|}+\frac{\left\|\boldsymbol{r}_{\zeta_i}^{\mathrm{II}}\right\|}{\|\boldsymbol{m}\|^4}\left[\boldsymbol{m}\odot(\boldsymbol{r}_{\eta_i}^{\mathrm{II}}\times\boldsymbol{m})\right], \tag{79}$$

$$\frac{\partial^2\theta_1}{\partial\mathbf{r}_{\eta_i}^{\mathrm{III}}\partial\mathbf{r}_{\zeta_i}^{\mathrm{III}}}=\frac{\boldsymbol{n}\otimes\mathbf{r}_{\eta_i}^{\mathrm{III}}}{\|\boldsymbol{n}\|^2\left\|\mathbf{r}_{\eta_i}^{\mathrm{III}}\right\|}+\frac{\left\|\mathbf{r}_{\eta_i}^{\mathrm{III}}\right\|}{\|\boldsymbol{n}\|^4}\left[\boldsymbol{n}\odot(\mathbf{r}_{\zeta_i}^{\mathrm{III}}\times\boldsymbol{n})\right], \tag{80}$$

$$\frac{\partial^2\theta_1}{\partial\mathbf{r}_{\eta_i}^{\mathrm{II}}\partial\mathbf{r}_{\zeta_i}^{\mathrm{III}}}=\mathbf{0}_{3\times3} \tag{81}$$

$$\frac{\partial^2\theta_1}{\partial(\mathbf{r}_{\zeta_i}^{\mathrm{II}})^2}==(A\frac{\partial^2\theta_1}{\partial\mathbf{r}_{\eta_i}^{\mathrm{III}}\partial\mathbf{r}_{\zeta_i}^{\mathrm{III}}}+\frac{\partial\theta_1}{\partial\mathbf{r}_{\zeta_i}^{\mathrm{III}}}\otimes\frac{\partial\theta_1}{\partial\mathbf{r}_{\eta_i}^{\mathrm{III}}})-(B\frac{\partial^2\theta_1}{\partial\mathbf{r}_{\eta_i}^{\mathrm{II}}\partial\mathbf{r}_{\zeta_i}^{\mathrm{II}}}+\frac{\partial\theta_1}{\partial\mathbf{r}_{\eta_i}^{\mathrm{II}}}\otimes\frac{\partial\theta_1}{\partial\mathbf{r}_{\zeta_i}^{\mathrm{II}}}), \tag{82}$$

Here, the symbol $\mathbf{0}_{3\times3}$ means a 3 × 3 zero matrix.

Owing to symmetry, the other 3 blocks of the Hessian matrix can be completed with the following identities

$$\frac{\partial^2\theta_1}{\partial\mathbf{r}_{\eta_i}^{\mathrm{II}}\partial\mathbf{r}_{\zeta_i}^{\mathrm{II}}}=(\frac{\partial^2\theta_1}{\partial\mathbf{r}_{\zeta_i}^{\mathrm{II}}\partial\mathbf{r}_{\eta_i}^{\mathrm{II}}})^T, \tag{83}$$

$$\frac{\partial^2\theta_1}{\partial\mathbf{r}_{\eta_i}^{\mathrm{III}}\partial\mathbf{r}_{\zeta_i}^{\mathrm{III}}}=(\frac{\partial^2\theta_1}{\partial\mathbf{r}_{\eta_i}^{\mathrm{III}}\partial\mathbf{r}_{\zeta_i}^{\mathrm{III}}})^T, \tag{84}$$

$$\frac{\partial^2\theta_1}{\partial\mathbf{r}_{\eta_i}^{\mathrm{II}}\partial\mathbf{r}_{\zeta_i}^{\mathrm{III}}}=(\frac{\partial^2\theta_1}{\partial\mathbf{r}_{\zeta_i}^{\mathrm{III}}\partial\mathbf{r}_{\eta_i}^{\mathrm{II}}})^T, \tag{85}$$